18th AIAA/CEAS Aeroacoustics Conference (33rd AIAA Aeroacoustics Conference)
04 - 06 June 2012, Colorado Springs, CO

AIAA 2012-2107

A High-Fidelity CFD/BEM Methodology For Launch Pad Acoustic Environment Prediction

Abhijit Tosh*, Peter Liever†, Fritz Owens‡
CFD Research Corporation, Huntsville, Alabama, USA

and

Yijun Liu§
Univ. of Cincinnati, School of Dynamic Systems, Cincinnati, Ohio, USA

The high-intensity level acoustic load generated by large launch vehicle lift-off propulsion is of major concern for the integrity of the launch complex and the vehicle payloads. This paper presents a practically feasible and effective computational process addressing the physics of both the noise generation mechanism and its footprint in the complex launch pad environment. High-resolution CFD solutions are coupled with a non-dissipative acoustic Boundary Element Method (BEM). The CFD/BEM interfacing approach involves identification of the noise sources and transformation of near-field noise signature to the acoustic solver. This approach is benchmarked against free and impinging jet problems prior to realistic application to the launch vehicle lift-off scenario.

I. Introduction

The vibro-acoustic environment induced by acoustic energy resulting from a propulsion system of large launch vehicles during lift-off is of great concern for the integrity of the launch complex, the vehicle itself and the vehicle payloads. Acoustic loads of 160dB to 200dB may reach sections of the launch vehicle, severely threatening the integrity of avionics systems or payloads.

The launch vehicle noise originates from the supersonic rocket plumes, which convert a small portion of the propulsive energy to acoustic energy that radiates from the outer boundary of the plumes. Noise from supersonic rocket plume small scale turbulence radiates uni-directionally, while highly energetic Mach wave radiation has a strong aft-ward direction[1]. The interaction and reflection of these highly energetic and directional waves from the launch facility structures back towards the vehicle are the main mechanisms for the high acoustic loads reaching the vehicle.

---

* Principal Engineer, AIAA Senior Member
† Technical Fellow, AIAA Senior Member
‡ Manager
§ Professor, College of Engineering & Applied Science

Copyright © 2012 by the American Institute of Aeronautics and Astronautics, Inc. All rights reserved.

Engineering models based on empirical jet acoustic strength and directivity models[2] (SP-8072) or scaled Saturn V measurements such as in the VAEPP (Vehicle Acoustic Environmental Prediction Program) are current state-of-the-art production tools[3]. These methodologies cannot account for deviations from the original data used in the empirical models.

Computational Fluid Dynamics (CFD) methods are now powerful and capable of running large-scale models using thousands of processors. CFD analyses of complete launch vehicles with multiple plumes interacting with full launch pad geometric models are performed by NASA engineers at Marshall Space Flight Center (MSFC). These analyses help define liftoff environments for the Shuttle and future NASA lift launch vehicle designs. Simulations with these tools in a time-dependent fashion with hybrid RANS/LES turbulence models can capture the sources of acoustic waves originating from the plumes and their propagation and interaction with the facility structures.

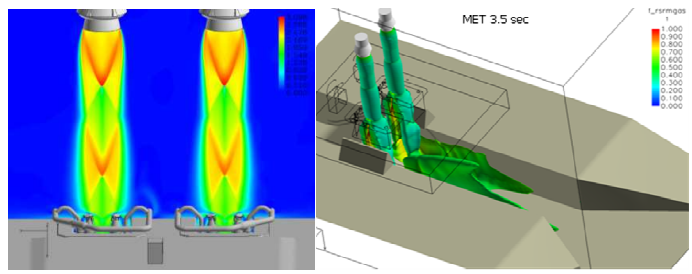

Figure 1. CFD analysis of launch vehicle lift-off Courtesy: NASA/MSFC, Fluid Dynamics Branch

While CFD tools are capable of simulating the details of internal plume structure and turbulent plume physics, they are numerically too dissipative for correctly propagating the acoustic waves over the large far-field distances, such as to the payload section at the tip of the vehicle. The computational cost of resolving the large space between the noise sources near the launch pad and the top of the launch vehicle with a grid resolution adequate for tracking the pressure waves accurately will be prohibitive in the near future. The surface integral methods (e.g. Ffowcs-Williams and Hawkings analogy[4]) that predict far-field noise (using free-space Green's functions) by post processing CFD solutions cannot be used for the liftoff acoustics application due to wave reflections from immersed solid surfaces in the propagation region.

The ideal capability to handle such complexity should be a single simulation method for accurate noise source and preservation of the acoustic waves at the same time. However, the current CPU power makes this approach prohibitively expensive and restricts us to a two-step approach. An accurate acoustic field can be obtained through dispersion preservation schemes[5], however without practical feasibility for large domains due to the constraints of high-order spatial and temporal schemes[6,7]. An appropriate alternative is to solve the Helmholtz equation, which can excellently preserve acoustic waves over long distances and provide the unsteady structural loading very efficiently[8,9,10].

In this paper, a coupled CFD/BEM approach is presented to unify high-fidelity near-field noise strength and frequency content and far-field noise propagation without numerical dissipation. This methodology is developed with a primary objective to provide accurate acoustic load distributions on the vehicle and launch pad structures.

II. Technical Methodology

The computational approach for noise calculations consists of two steps of physics modeling and simulations. In the plume flow near-field region, the sound pressure wave sources are generated by shock cell structures and nonlinear, turbulent, multi-species, fluid mixing processes. This physics is governed by the unsteady compressible Navier-Stokes equations simulated using a hybrid RANS/LES model for turbulence. The acoustic far-field fluid dynamics environment is predominantly linear and irrotational and the simulation of noise propagation is performed with an efficient and highly accurate wave propagation method based on an acoustic BEM model. Two distinct characteristics of sound can therefore be considered: (1) the nonlinear generation of sound, and (2) the linear propagation of sound. The separation of the problem into linear and nonlinear regions allows the use of the most appropriate numerical methodology for each. This approach has been the basis for all current development of Computational Aero-Acoustic (CAA) methodologies.

CFD/BEM interfacing

An interfacing control surface sub-dividing the computational domain is selected such that it encloses all the nonlinear flow effects and noise sources as shown in Figure 2. This approach is also taken widely for surface integral methods[11], and BEM as well. This interface enables coupling of two highly established and high-fidelity computational tools viz., Loci/CHEM[12] (developed by Prof. Ed Luke at Mississippi State University) and FastBEM[13] (developed by Prof. Yijun Liu at University of Cincinnati). A flow diagram of the interfacing process is shown in Figure 3.

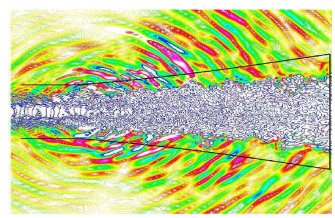

Figure 2. Control surface around jet flow

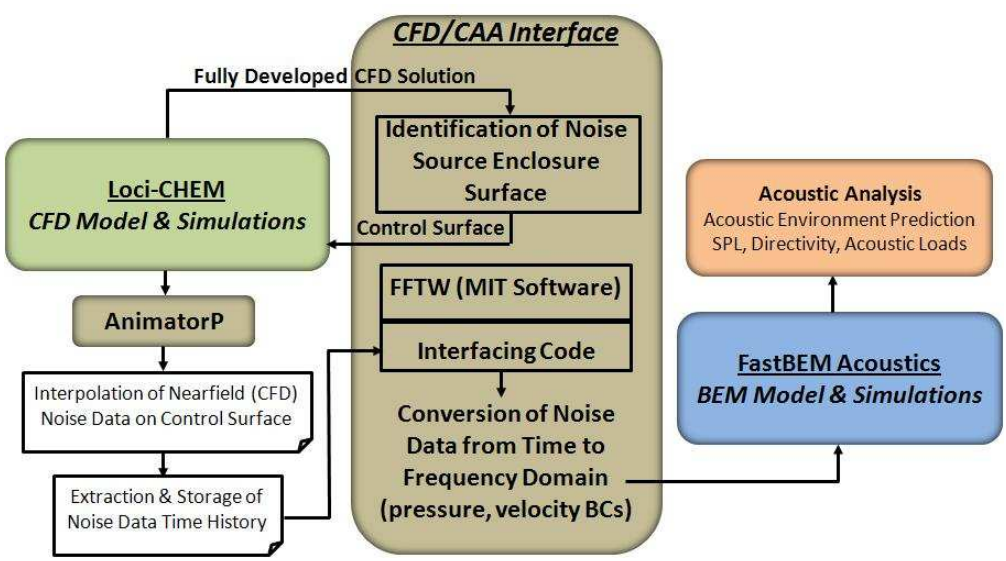

Figure 3. CFD/CAA simulation approach

In the early phases of this work the noise source enclosing surface was identified by scrutinizing various flow variables of the fully developed instantaneous CFD solutions, such as the velocity divergence, pressure fields and also by taking insights from the general practice involved in selecting these domains[14,15]. In a subsequent section, an approach for automating the noise source extraction process will be described. Once the surface has been identified, mesh points are generated on tthe surface and provided to the CFD solver in order to store a time history of instantaneous solutions for each point on the surface. The time domain CFD solution is then transformed into frequency domain using a Discrete Fourier Transform (DFT) software[16] (developed by Matteo Frigo and Steven G. Johnson at MIT). The FastBEM input is thus generated from the knowledge of the noise amplitude and frequency content of the near-field noise source enclosure surface.

Acoustic Boundary Element Method (BEM)

The BEM formulation is based on the Helmholtz equation for time-harmonic acoustic waves that can be transformed into a boundary integral equation (BIE). The corresponding BIE is given by

$$c(\mathbf{x})\phi(\mathbf{x}) = \int_S \left[G(\mathbf{x},\mathbf{y},\omega)q(\mathbf{y}) - F(\mathbf{x},\mathbf{y},\omega)\phi(\mathbf{y})\right] dS(\mathbf{y}) + \phi^I(\mathbf{x}) + QG(\mathbf{x},\mathbf{x}_Q,\omega), \quad \forall \mathbf{x} \in S \tag{1}$$

in which ϕ is the acoustic pressure, S the surface of the structure V, constant $c(\mathbf{x})$ = ½ if S is smooth around the point $\mathbf{x}$, $q = \partial\phi/\partial n$, ϕ^I the incident wave, and the two kernels (Green's functions) are:

$$G(\mathbf{x},\mathbf{y},\omega) = \frac{1}{4\pi r} e^{ikr}, \qquad F(\mathbf{x},\mathbf{y},\omega) \equiv \frac{\partial G(\mathbf{x},\mathbf{y},\omega)}{\partial n(\mathbf{y})} \tag{2}$$

for 3-D full-space problems, with $i = \sqrt{-1}$, ω the frequency, r = the distance between points $\mathbf{x}$ and $\mathbf{y}$. BIE (1) can be employed to solve for the unknown ϕ and q on S. The term $QG(\mathbf{x},\mathbf{x}_Q,\omega)$ represents the contribution of a typical monopole point source located at $\mathbf{x}_Q$ (inside the acoustic domain E) with Q being the complex amplitude of the source.

Once the acoustic pressure ϕ and q on S are obtained using the BEM, the values of ϕ at any point $\mathbf{x}$ inside the domain E can be determined by applying the following representation integral:

$$\phi(\mathbf{x}) = \int_S \left[G(\mathbf{x},\mathbf{y},\omega)q(\mathbf{y}) - F(\mathbf{x},\mathbf{y},\omega)\phi(\mathbf{y})\right] dS(\mathbf{y}) + \phi^I(\mathbf{x}) + QG(\mathbf{x},\mathbf{x}_Q,\omega), \quad \forall \mathbf{x} \in E \tag{3}$$

which can be regarded as a post-processing step in the BEM solution. A dual BIE formulation is used in the *FastBEM Acoustics* code so that the so called *fictitious eigenfrequency* difficulties do not exist when solving exterior acoustic problems.

The discretized equations of the BIE (1) can be obtained by discretizing the boundary S using boundary elements. With constant elements, all the singular and hypersingular integrals in the BIE can be evaluated analytically, which is much more efficient and accurate than computing these singular integrals with numerical quadrature.

A conventional BEM approach for solving the BIEs is in general slow and inefficient for large-scale BEM problems, despite its robustness in the modeling or meshing stage as compared with other domain based methods. For a PC with 2 GB memory, the largest BEM models can be solved using the traditional, straightforward BEM approach can have at most about 10,000 unknowns (DOFs). This is a severe limitation on the BEM for modeling acoustic problems with complicated domains and at higher frequencies. The *FastBEM Acoustics* code, on the other hand is based on the fast multipole method, which can be employed to accelerate the solutions of the BEM systems of equations dramatically. Near $O(N)$ computational efficiencies can be achieved in solving the BEM models by applying the FMM with the BEM.

III. Results and Discussion

In order to establish for the validity of the coupled CFD/BEM approach for HLV aeroacoustics in the launch pad architecture, it is necessary to assess the accuracy of the noise prediction through suitable benchmark problems. Noise generated by vortex shedding from a cylinder is a common test case and hence is considered for assessment of this hybrid approach. Numerous jet noise experiments can be found for both free and impinging jets, hot/cold, supersonic/subsonic as well, that are relevant to the HLV aeroacoustics[17,18] problem. The quality of near-field predictions has a strong reflection in the Overall Sound Pressure Level (OASPL) predictions and directivity patterns to the far-field using the acoustic BEM. Hence, both methods need to be evaluated in order to establish a confidence level of the overall aeroacoustic approach.

Noise radiation by vortex shedding from flow over a cylinder

Cox et al.[19] report computational results of both the fluid dynamics and the acoustic wave propagation comparing against experimental observations[20]. This test case consisted of flow past a cylinder at a Reynolds number of 89,000 and a Mach number of 0.2 at atmospheric pressure. The cylinder length to diameter ratio was 26. The experimental apparatus is depicted in Figure 4a and the Sound Pressure Level recorded at the microphone location at 128 diameters from the cylinder is shown in Figure 4b.

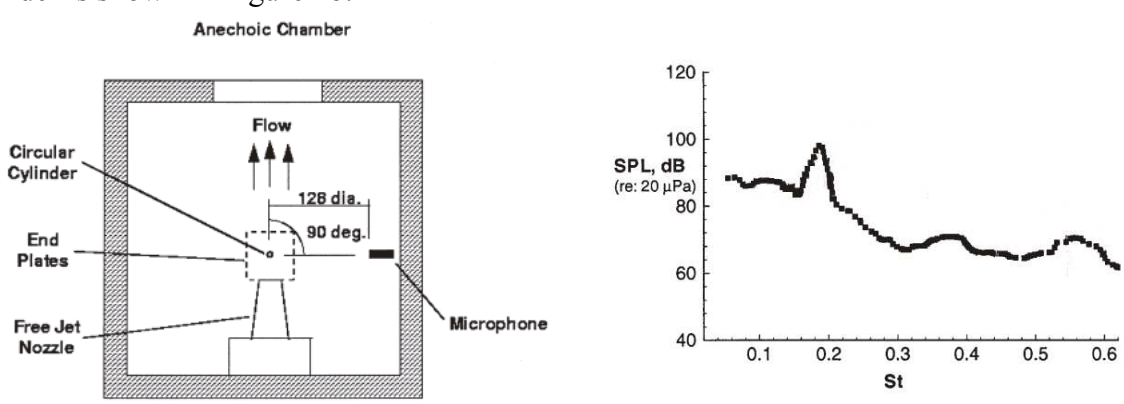

a. Schematic of experimental setup b. Sound pressure level recorded

Figure 4. Experimental setup and measurements for Re = 89,000

It is important to note that both three-dimensional effects and transition to turbulence contribute to the flow structure and noise generation at this Reynolds number. Nonetheless, the noise generated at the fundamental shedding frequency (Strouhal number of 0.17) is 15-20 dB above the broader noise spectrum.

The CFD simulation was performed with CFD-ACE+. The calculation domain was annular in shape with an inner radius of D/2 where D is the cylinder diameter and an outer radius of 31D. The mesh contained 49,162 cells closely spaced near the cylinder surface and arranged more densely in the wake than in the upstream region. A laminar flow simulation was performed and was run for a sufficiently long time that the shedding behavior had reached periodic behavior. A snapshot of the x-direction velocity field after the periodic shedding behavior had been obtained is shown in Figure 5. The predicted values of the x-direction velocity at a location in the near-wake region are shown in Figure 6. The resulting Strouhal number is 0.185 which should be compared to the experimental value of 0.17.

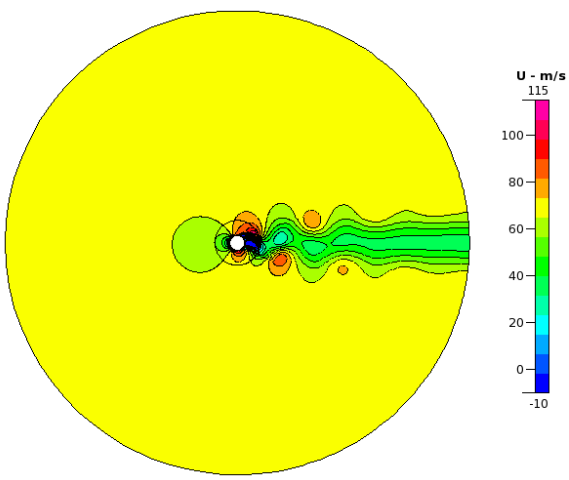

Figure 5. Instantaneous velocity field for vortex shedding flow past a cylinder

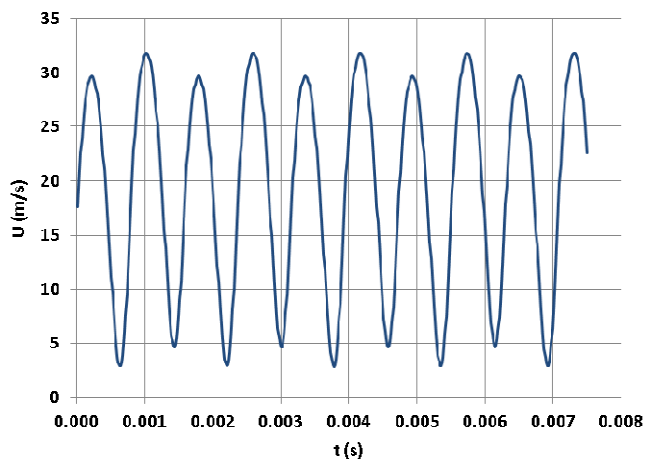

Figure 6. Variation of velocity in the near wake region over several shedding cycles

The acoustic mesh consisted of 38400 triangular boundary elements. A graphical depiction of Sound Pressure Level (SPL) predicted by that simulation is shown in Figure 7, in which the cylinder is surrounded by a concentric annulus with inner radius of 120D and an outer radius of 130D. These annuli are "field point" surfaces on which FastBEM calculates the local solution values after the overall BEM solution has been obtained using the boundary conditions on the cylinder. The smaller ring is useful to display the solution in the vicinity of the cylinder and the larger one is required in order to obtain the solution at a distance of 128D from the cylinder (corresponding to the measurement location in the experiments of Revell[20] and the directivity predictions of Cox[19]). The SPL at the 128D radius is shown in Figure 8 along with simulation results obtained by Cox et al[19]. Note that the laminar flow prediction of Cox et al. is for a Reynolds number of 1000 and is included by them only as a representative laminar solution. The turbulent solution using the Shear Stress Transport (SST) turbulence model is their preferred solution. The directivity of the predicted SPL field seems to match well with that of Cox. The value of the SPL at an angle of 90º is 102.5 which compares very favorably to the experimental

value of about 98 shown in Figure 4b and in Figure 8a. The current simulation should predict a higher SPL because the acoustic energy is contained entirely in the shedding frequency while that in the experiment is spread across a broader spectrum.

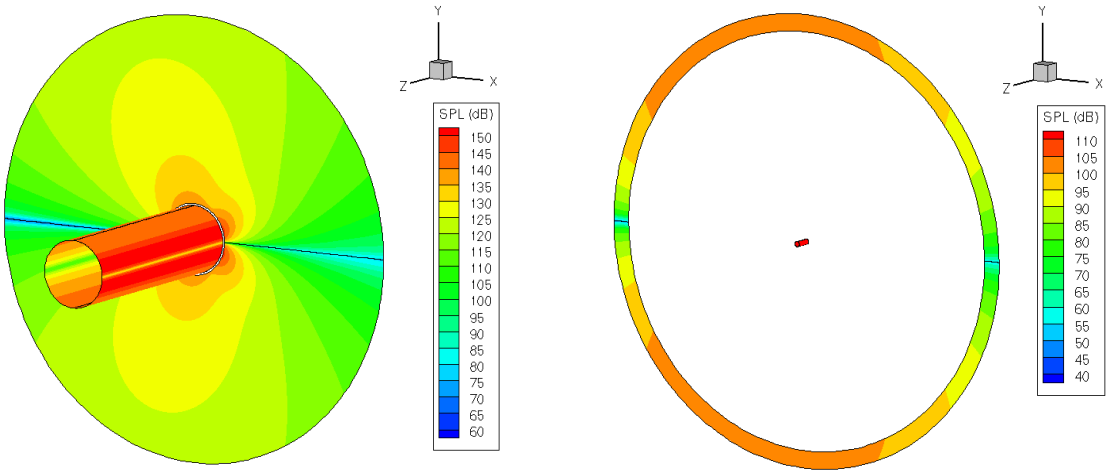

a. SPL in near-field b. SPL in far-field

Figure 7. FastBEM predictions of noise (SPL dB ref:20μPa) in the near-field and far-field

Also, the difference between the predicted SPL at 90º of 102.5 and the value of about 93 predicted by Cox et al., can be attributed to the fact that the current acoustic model was for a cylinder of length 20D and implicitly assumes fully correlated vortex shedding along the entire length. Cox et al. performed their calculations for a cylinder length of 5D as a better representation of actual correlation lengths and demonstrated that this would result in lower values of sound pressure level than would a longer cylinder length.

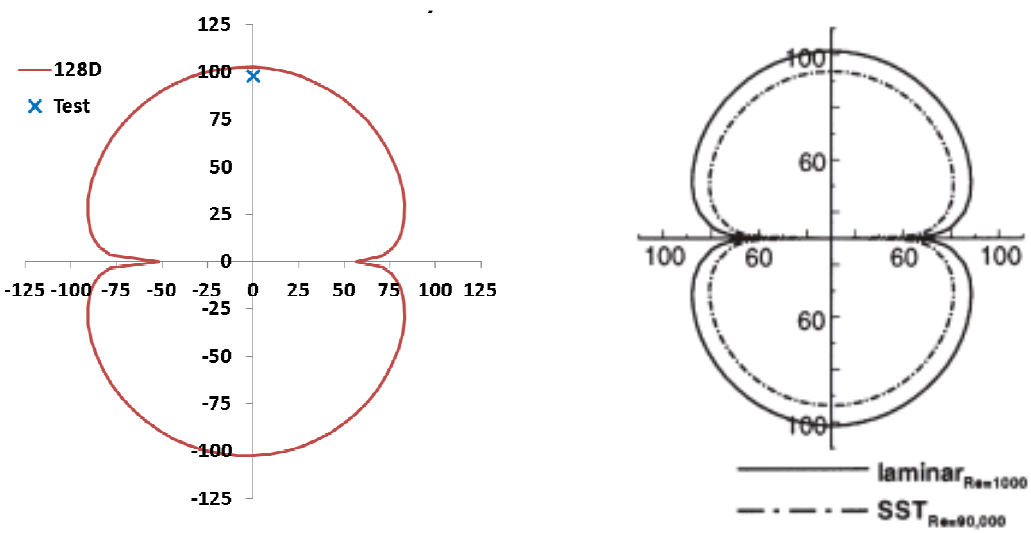

a. Results of FastBEM. b. Results of Cox et al.

Figure 8. Directivity pattern predicted by FastBEM and by Cox et al.

Jet impingement noise from SHJAR

The second case simulated was the sound wave production from supersonic jet impingement on a flat surface. Experiments were performed at the Small Hot Jet Aeroacoustics Rig (SHJAR) at NASA Glenn and (limited) data is available for comparison with the model predictions[21,22]. In the experiments a Mach 2.0 supersonic jet with a nozzle diameter of d=1.0 inch impinges normally on a flat plate at varying standoff distances, h. The impingement produces an intense discrete frequency screech sound. The frequency of the screech tone is dependent on the h/d ratio and occurs at approximately 8000 Hz for h/d=2.5.

The CFD simulation of this jet was performed at NASA using the Loci/CHEM flow solver[23]. A time-accurate unsteady RANS simulation was performed. The 3-D computational model consisted of 33M cells that were primarily tetrahedral although prism cells were extruded from the solid surfaces in order to better resolve boundary layers. Figure 9 visualizes the fields of velocity divergence and pressure with very strong directional screech tone noise waves originating from the jet shear layer impingement region.

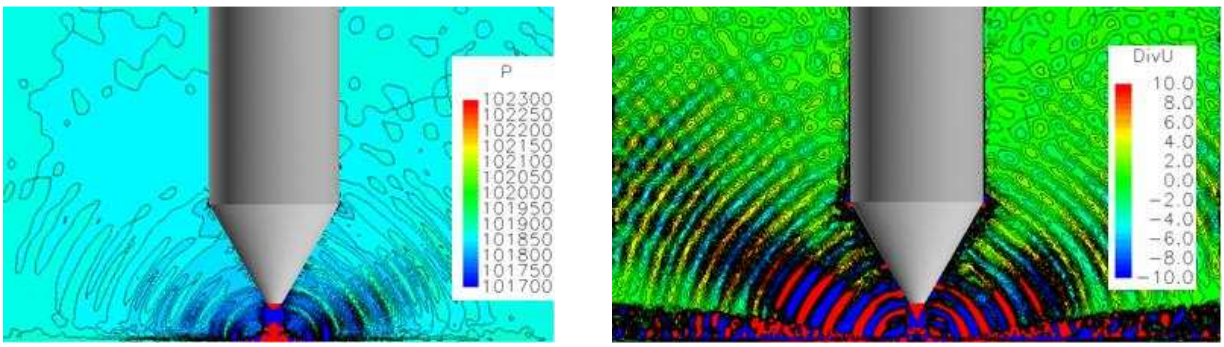

(a) Contours of pressure (b) Contours of divergence of velocity

Figure 9. CFD solutions of supersonic impinging jet acoustical field

Examination of the CFD solution data revealed that the contours of ω, the specific dissipation rate of turbulence kinetic energy, were very well aligned with the shear layers surrounding the high speed flow. Thus, a suitable contour value of ω was chosen to create a noise control surface as shown in Figure 10.

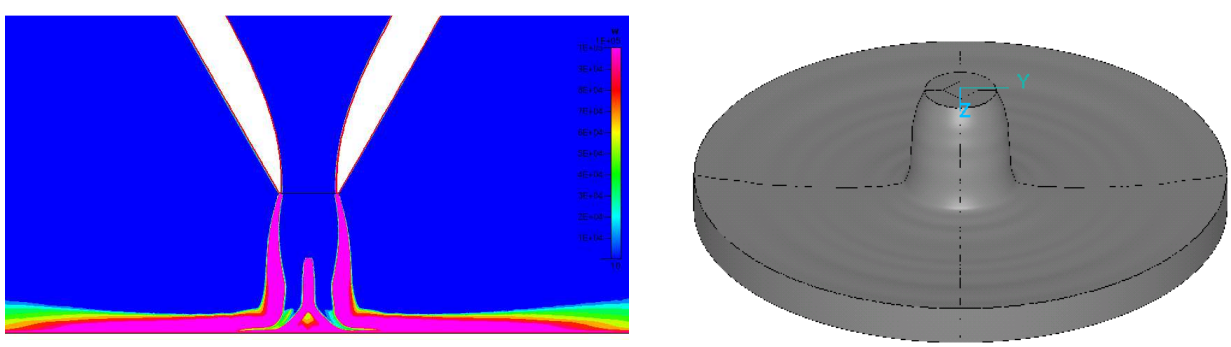

Figure 10. Contours of ω and the interface surface derived from the ω field

The boundary conditions for FastBEM were taken from the CFD simulations by interpolation to the interface mesh at 300 time intervals with a time step size of 10^{-5} s. The data on the interface mesh were then transformed to the frequency domain and used to prepare input decks for FastBEM simulations at 24 frequencies from 500 Hz to 12000 Hz. The mesh size of the CFD simulation and the interface surface determine the maximum frequency that can be resolved by the CFD and, consequently, the acoustic simulation in FastBEM. The is because both the CFD and the acoustic simulations require a certain number of mesh points, typically 6 to 10, to resolve a single wavelength. The CFD mesh has resolution of about 0.5 mm in the region surrounding the jet prior to impingement while the interface surface mesh has 0.5 mm x 1.2 mm resolution in the same area. Both meshes become coarser as the flow turns outward radially and a reasonable limiting mesh size is taken as 2 mm. Additionally, the computational time step places limits on both the minimum and maximum frequencies that can be resolved. These limits are shown in Table 1, which shows that the maximum frequency limit is dictated by the mesh size.

Table 1. Minimum and maximum frequencies that can be predicted

	Minimum frequency	Maximum frequency
Mesh size (2 mm) limit	-	17,150 Hz
Number of time steps (200) limit	-	50,000 Hz
Sampling duration (2 ms) limit	500 Hz	-

FastBEM simulations were carried out using pressure boundary conditions at frequencies from 1000 to 12,000 Hz and were converged to a normalized residual level of 3.5×10^{-4}. Figure 11 shows a three-dimensional view of the FastBEM domain consisting of the interface or source surface on which the boundary conditions were extracted from the CFD simulation. Two additional planes in the Cartesian xy-plane have been added for display of the simulation results. Results of the various simulations will typically be shown in views looking along the z-axis at the xy-plane.

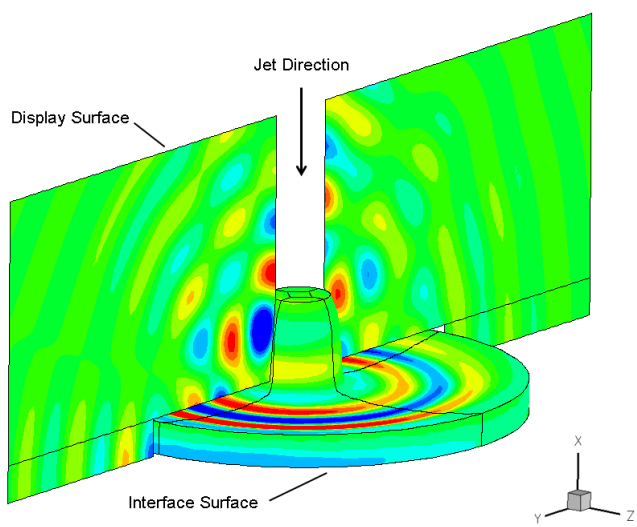

Figure 11. FastBEM boundary and simulation results in the XY-plane

.
Typical acoustic spectrum results for an impinging jet case are shown in Figure 12. These results were for h/d = 2.02 rather than h/d = 2.5 and as a result the frequency peak occurs at approximately 10,000 Hz. For h/d = 2.5 the frequency peak is known to occur at approximately 8000 Hz. It is presumed that the broadband noise spectrum is the same for the two configurations. FastBEM simulation results at 8000 Hz are shown in terms of the SPL in Figure 13 and the real part of the pressure field is shown in Figure 14. The predicted spectrum shows fair agreement with the experimental results. In Figure 13 the peak is spread over the 8000 to 9000 Hz interval rather than being concentrated very near a single frequency. The difference between the peak and the broader spectrum is similar in the simulation and the data.

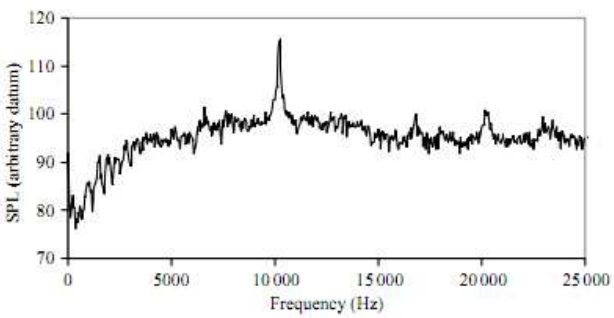

Figure 12. Far-field spectrum for h/d = 2.08. Measurement at an angle of 30º from the upstream jet axis and 0.5 m from the impingement plate

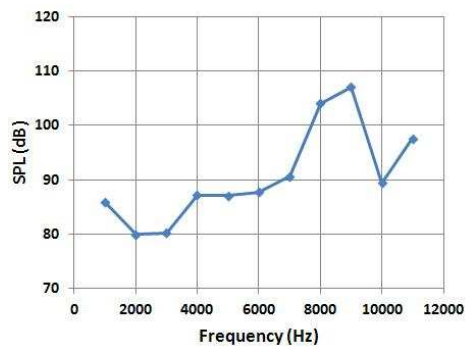

Figure 13. FastBEM predictions of SPL over range of frequencies (dB ref:20μPa)

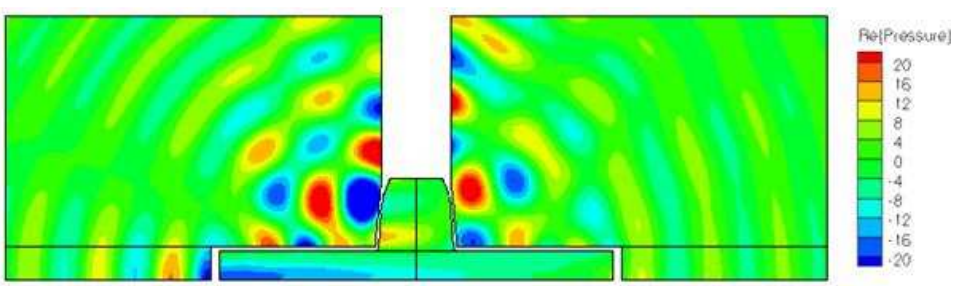

Figure 14. Real part of pressure field at 8000 Hz

The Seiner supersonic free jet noise

This section presents a supersonic free jet plume simulation of an experiment performed at the NASA Langley Research Center (LaRC) Jet Noise Laboratory[24]. This case, commonly referred to as the Seiner jet, is widely used for validation of Kirchhoff and FWH noise propagation methods. It constitutes one of the standard validation cases for supersonic jet Mach wave noise patterns. These experiments investigated an axisymmetric water-cooled Mach 2 nozzle with an exit diameter of D = 3.60 in. (91.44 mm) operating at perfectly expanded conditions for Mach = 2 exit flow. The jet stagnation condition has a total temperature of T_t = 2000°F = 1370K. The ambient pressure is P_{amb} = 14.91 psia = 102800 Pa.

The simulation was performed with the Loci/CHEM code using a hybrid RANS/LES modeling approach with the Menter-SST model used for the RANS model. The solution was time-dependent with a time step size of 10^{-5} s. The CFD mesh used for the Seiner jet simulation consists of approximately 72 million cells with the finest mesh within and around the jet. Mesh resolution in that region is approximately 5 mm. In order to avoid spurious wave reflections from the outflow boundary, a buffer zone is created in the far downstream region with much relaxed mesh density compared to the jet core and the turbulence mixing region.

Figure 15 illustrates the unsteady flow physics of this supersonic jet through instantaneous contour plots (on a mid plane through the center of the jet). Intense Mach wave generation can be seen at the end of potential jet core where the strength of the shock cells gradually decays and finally breaks down into a turbulent mixing zone. The Kelvin-Helmholtz instability waves within the shear layers and their growth while propagating downstream can be clearly observed in the pressure contours and the close up snapshot of the divergence of velocity field as well.

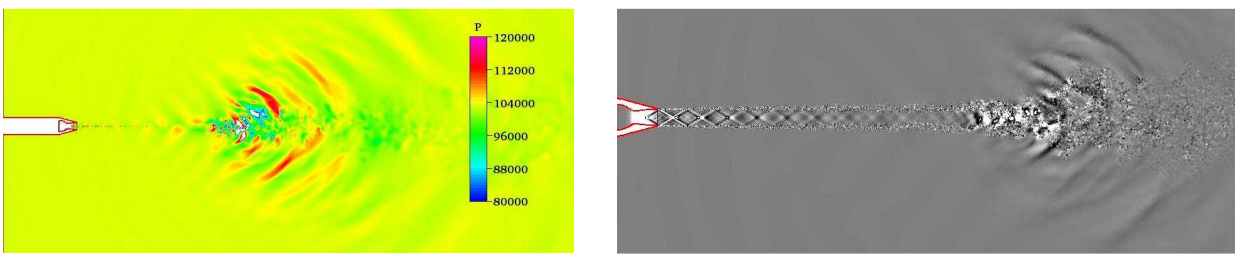

(a) Pressure contours (b) Divergence of velocity

Figure 15. CFD solutions of supersonic jet plume flow

The near-field noise characteristics captured by the CFD simulation can also be comprehended from the contours in Figure 15. The pressure waves, however, quickly dissipate due to coarser mesh density both in the radial and downstream directions away from the jet. The noise enclosure surface was defined based on studying the extent of major noise contributing regions from the contour plots of CFD solutions (axial velocity, divergence of velocity, and pressure fields etc.), CFD mesh density and extension in the radial direction (Figure 16). It is also important to place the surface within the acoustically non-dissipative region of the CFD mesh. Several references were all consulted for guidance in selecting the control surface for free jet as well[25,26,27]. The starting vertical (normal to the jet axis) surface location was located at $0.25\times D_{jet}$ from the nozzle exit plane. The starting diameter of the enclosure surface was set at $1.41\times D_{jet}$, and the diameter expanded to $2.0\times D_{jet}$ at the axial location $20.0\times D_{jet}$ (refer to literature above). The second part of the source enclosure surface is considered by analyzing the contour plots of all the flow quantities.

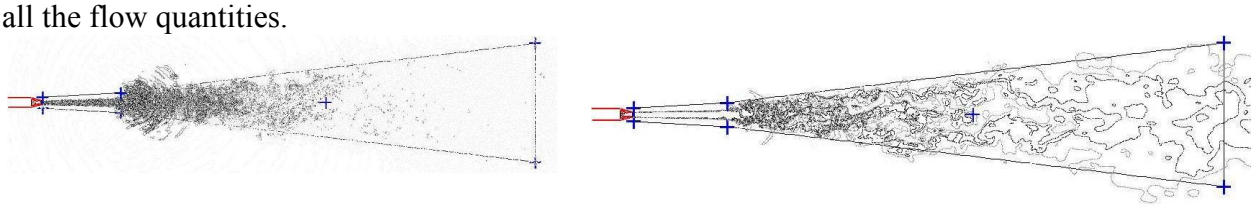

(a) Divergence of Velocity Contours (b) Axial Velocity Contours

Figure 16. Noise source surface with flow contour lines

As mentioned previously the mesh resolution is about 0.005 m in the near-jet region. The simulation was performed with time steps of 10^{-5} seconds and data was extracted at 1000 consecutive time steps although only 500 were used for transformation to the frequency domain. The spatial and temporal resolutions of the CFD solution impose limits on the minimum and maximum frequencies that we can obtain from the solution. The spatial resolution imposes one limit on the maximum frequency. Assuming that we can resolve a single wavelength with 10 cells the smallest wavelength we can resolve is 0.05 m and the highest frequency is $c/\lambda = 6860$ Hz. The temporal resolution of the solution determines the lowest frequency we can resolve and also, along with the number of samples or data points, the maximum frequency. The lowest frequency will be 1/T (where T is the total period over which the samples were taken) and the highest frequency will be N/(2T) where N is the number of samples. Thus, we can resolve frequencies as low as 200 Hz and as high as 50 kHz based just on the temporal resolution. However, the spatial resolution places an upper limit of less than 7 kHz and that will be the controlling limit.

The noise surface mesh resolution also imposes a limit since it is the boundary mesh used in FastBEM. The axial mesh size of that mesh is approximately 0.015 m where the mesh has its smallest radius and increases as the radius of the surface increases. Based on this dimension and relaxing our mesh requirement to accept a minimum of six cells to resolve a single wavelength the smallest wavelength we can resolve in FastBEM is about 0.09 m and the highest frequency is about 3800 Hz. Thus we can expect our prediction of the far-field noise to be best in the range from 200 to 3800 Hz (see Table 2). After transformation to a triangular element mesh the FastBEM model consisted of 104,880 boundary elements. FastBEM simulations were carried out using both pressure and velocity as boundary conditions (in separate simulations) at frequencies from 200 to 3000 Hz and were converged to a normalized residual level of 3.5×10^{-4}. The real part of the pressure field is shown in Figure 17a and the Sound Pressure Level is shown in Figure 17b from simulations at 1400 Hz.

Table 2. Minimum and maximum frequencies that can be predicted for Seiner jet

	Minimum frequency	Maximum frequency
Mesh size (9 mm) limit	-	3800 Hz
Number of time steps (500) limit	-	50,000 Hz
Sampling duration (5 ms) limit	200 Hz	-

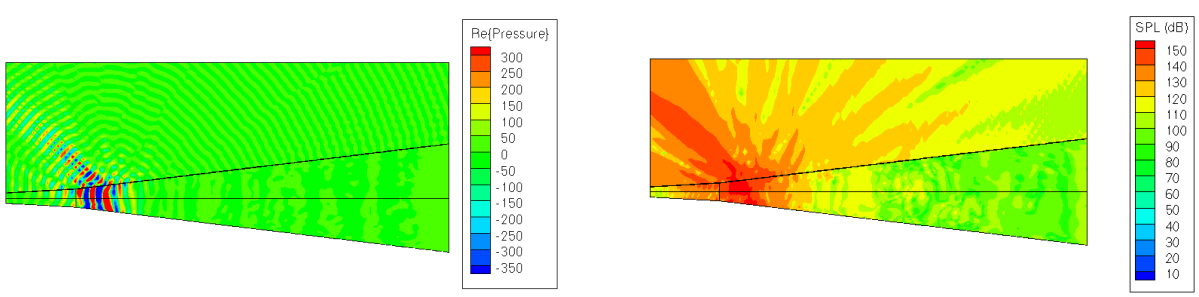

(a) Real part of pressure field (b) Sound Pressure Level

Figure 17. Real part of pressure and SPL (dB ref:20μPa) field at 1400 Hz

Seiner jet acoustic measurements were taken at the locations designated as the L array, presented as far-field data, and the N array, presented as near-field data. The L array of microphones were physically laid out in an L shape but the report notes that: "all far field data presented is corrected to a 3.66 meter distance on a circular arc centered at the nozzle exit." Therefore, the solution data is sampled at the locations shown in Figure 18 for comparison with the reported Seiner jet data.

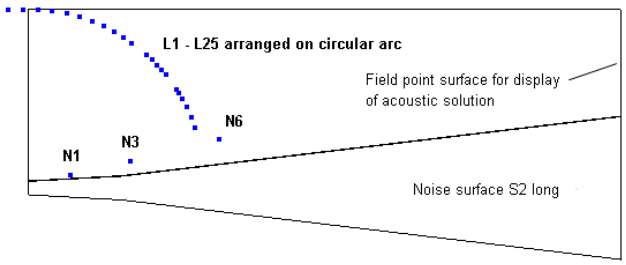

Figure 18. Locations at which solution data was sampled

The FastBEM solution is compared with the data reported in Seiner in the following figures. Far-field and near-field spectra at different locations and angles are shown in Figures 19 and 20. The continuous line labeled "Data" is the experimental data and the discrete data points were taken from the FastBEM simulations. The experimental data was digitized from Seiner et al.

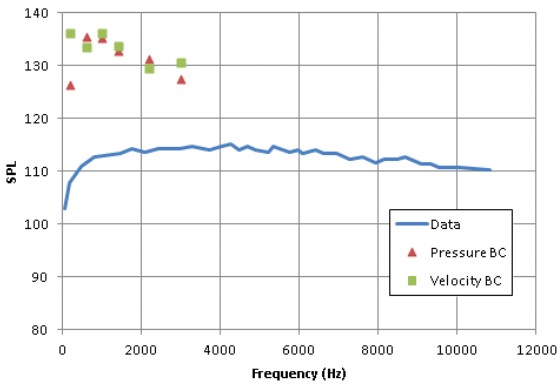

(a) SPL at an Angle 88.56°

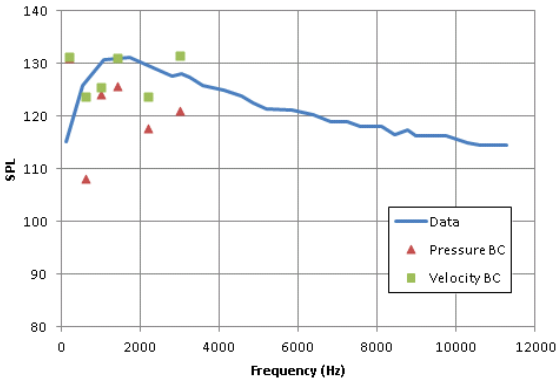

(b) SPL at an Angle of 128.94°

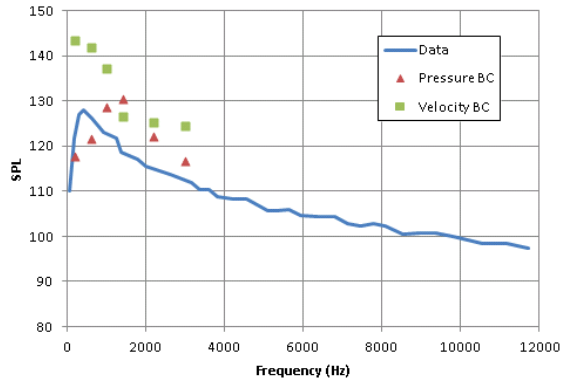

(c) SPL at an Angle of 160.1°

Figure 19. Comparison of predicted and measured far-field SPL

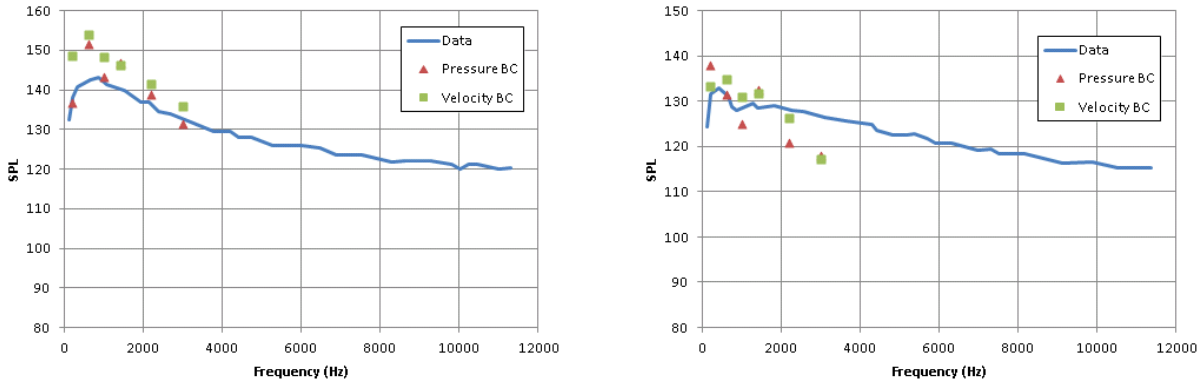

(a) SPL at Near-Field Point N3 (b) SPL at Near-Field Point N6

Figure 20. Comparison of predicted and measured near-field SPL

Overall, a fair degree of agreement is observed between the simulation results and the experimental. The greatest discrepancy is in the Sound Pressure Level at the angles less than, say, 130°. The highest SPL values predicted occur at about 90° and decrease to about 130° while the lowest measured values occur at about 90° and increase to beyond 130°. This excessive prediction of sound energy radiated in the upstream direction is predicted in Figure 19(a) at an observer angle 88.56°, where the most intense pressure variations are directed upstream from the vicinity of the potential core breakup region. Possible reasons for the discrepancy, to be investigated in future work, include:

- Low-order interpolation used for extraction of the CFD data on the noise source surface that could be improved by higher-order interpolation from surrounding CFD solution points.
- Improper placement of the noise source surface. Predicted pressure variations in the potential core region are quite large and it is possible that the noise source surface must be moved further away. One additional source surface was tried but it was not sufficiently far removed to avoid the large pressure variations.
- Incorrect CFD results for this case. The core breakup region is known to occur at a location 10D downstream of the jet exit (literature referred earlier in this section) but the CFD predicted it to occur at a distance of 20D. This is not an uncommon occurrence in high-speed jet simulations and potential remedies are known.
- Inconsistent boundary conditions used in the FastBEM simulation. The pressure and velocity boundary conditions are not necessarily consistent in the sense that FastBEM expects. An improved boundary condition treatment for FastBEM is needed.

Identification and preparation of noise source enclosure surface

In the aeroacoustic community, it is well known that the Lighthill's equation[28] uniquely describes the physics of aerodynamic sound generation and propagation. The source term of this equation provides valuable information for identification of the CFD/CAA interface. However, it is important to note that calculations of the right hand side source term of the Lighthill's equation

directly from CFD solution fields will contain the propagating acoustic field along with the core noise sources. This makes it difficult to obtain an iso-surface that represents only the noise sources (excluding the propagation).

Lighthill's equation $$\frac{\partial^2 \rho'}{\partial t^2} - c_0^2 \frac{\partial^2 \rho'}{\partial x_i^2} = \frac{\partial^2 T_{ij}}{\partial x_i \partial x_j} \tag{4}$$

where ρ' is the density field (fluctuation), c_0 is the speed of sound, and T_{ij} is the Lighthill's stress tensor that represent the sources of noise. The full form of the Lighthill's stress tensor is given as:

$$T_{ij} = \rho u_i u_j + \left\{ (p - p_0) - c_0^2 (\rho - \rho_0) \right\} \delta_{ij} - \sigma_{ij} \tag{5}$$

Figure 21 indicates that using the Lighthill's source term in CFD solutions, it is not possible to obtain an iso-surface that represents only the noise source region excluding the propagation field. The benchmark problems presented here were geometrically simpler in order to study the acoustic source region and generate corresponding noise surface enclosures. However, this process can become much complicated for complete vehicle launch system. Thus, it is desired to reduce the manual efforts in identifying and consequent construction of this surface. This process is described hereafter.

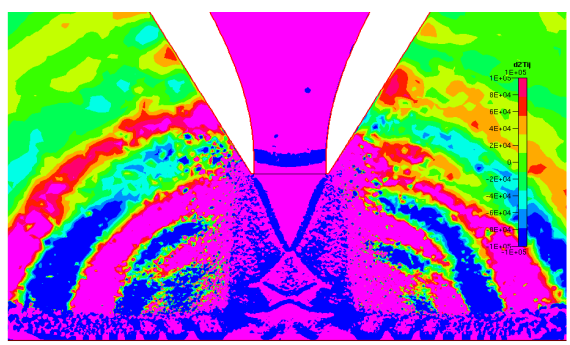

Figure 21. Contours of Lighthill's source term for SHJAR case

The first term being dominant as compared to the remaining two terms (entropy noise and viscous part), the stress tensor is commonly approximated as:

$$T_{ij} \approx \rho u_i u_j \tag{6}$$

The velocity field in this tensor is the total velocity. When the Reynolds decomposition of velocity field is introduced in the tensor, it evolves several components of the tensor with different physical interpretations[29].

Reynolds decomposition $$u_i = \overline{u_i} + u_i' \tag{7}$$

The various components evolved from the Lighthill's stress tensor by introducing Reynolds decomposition are:

$$T_{ij} = T_{ij}^{m} + T_{ij}^{l} + T_{ij}^{n} + T_{ij}^{s} \tag{8}$$

Where the components represent the following physical meaning:

Mean (does not produced noise) $$T_{ij}^{m} = \rho\overline{u_i}\,\overline{u_j} + \left(\overline{p} - c_0^2\overline{\rho}\right)\delta_{ij} \tag{9}$$

Linear velocity fluctuation $$T_{ij}^{l} = \rho\overline{u_i}u'_j + \rho\overline{u_j}u'_i \tag{10}$$

Quadratic velocity fluctuation $$T_{ij}^{n} = \rho u'_i u'_j \tag{11}$$

Entropy component $$T_{ij}^{s} = \left(p' - c_0^2\rho'\right)\delta_{ij} \tag{12}$$

Computation of these various components require information of the average flow fields. The fluctuating fields can then be obtained further instantaneous simulations. This process was not in the scope of the simulations presented in this paper. Hence in this work, the total quantities of the stress tensor from equation (6) were considered for the noise source extraction process. The Lighthill's stress tensor has nine components as shown below:

$$T_{ij} = \rho u_i u_j = \begin{bmatrix} T_{xx} & T_{xy} & T_{xz} \\ T_{yx} & T_{yy} & T_{yz} \\ T_{zx} & T_{zy} & T_{zz} \end{bmatrix} = \begin{bmatrix} \rho uu & \rho uv & \rho uw \\ \rho vu & \rho vv & \rho vw \\ \rho wu & \rho wv & \rho ww \end{bmatrix} \tag{13}$$

The individual components have directional effect on the noise sources. Thus, in order to obtain an overall scalar field of the stress term, only the diagonal components are considered here to get the following:

$$T_{ij,diag} = \sqrt{T_{xx}^2 + T_{yy}^2 + T_{zz}^2} \text{ and } T_{ij,mult} = \sqrt{T_x^2 + T_y^2 + T_z^2} \tag{14}$$

Where,

$$T_x = \sqrt{T_{xx}^2 + T_{xy}^2 + T_{xz}^2}\ ,\ T_y = \sqrt{T_{yx}^2 + T_{yy}^2 + T_{yz}^2}\ ,\ T_z = \sqrt{T_{zx}^2 + T_{zy}^2 + T_{zz}^2} \tag{15}$$

The Lighthill's stress tensor was calculated for the jet noise cases of Seiner free jet, SHJAR jet impingement and the ASMAT case as well. The iso-surfaces were obtained as shown in Figure 22.

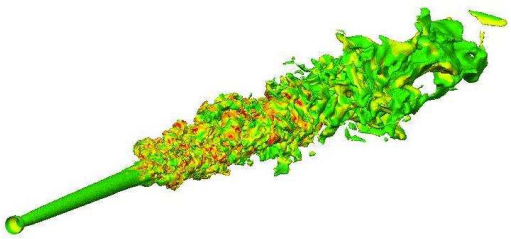

(a) Seiner Free Jet Noise: Iso-surface of Lighthill's Stress Tensor

($T_{ij,diag} = 10000$)

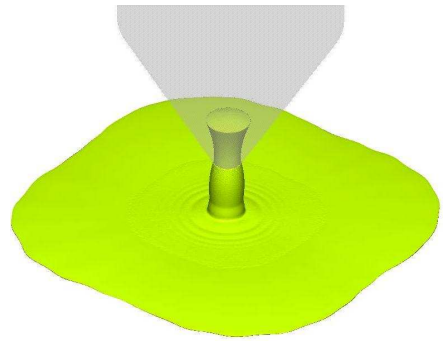

(b) SHJAR Jet Impingement Noise: Iso-surface of Lighthill's Stress Tensor

($T_{ij,diag} = 20000$)

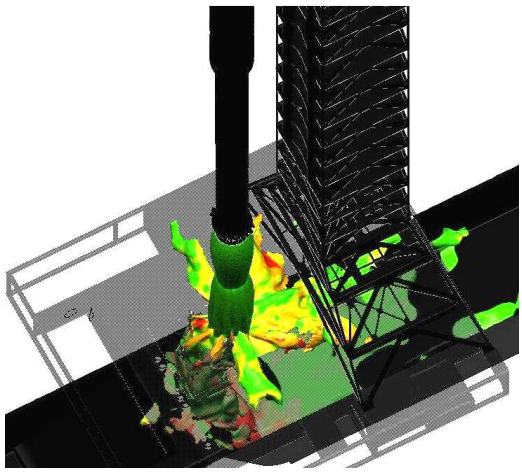

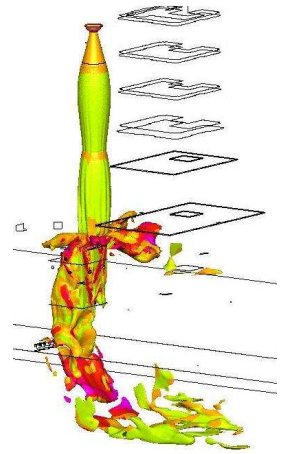

(c) ASMAT Jet Impingement Noise: Iso-surface of Lighthill's Stress Tensor ($T_{ij,diag} = 100000$, colored by $T_{ij,mult}$)

Figure 22. Demonstration of identification and preparation of noise source surfaces

It is demonstrated that using the Lighthill's stress tensor, iso-surfaces can be obtained that represent the noise generation region in a flow. Once such a surface is obtained, a noise source enclosure surface can be constructed around this iso-surface for near-field noise source extraction and acoustic BEM input.

IV. Conclusion

In this paper, a CFD/CAA approach is presented for predicting high speed flow-induced noise generation and the resulting acoustic signature. This approach unifies two production level high-fidelity physics models through an efficient technique for seamless interfacing of near-field noise emission to far-field propagation and its impact on the surrounding. Combination of these multi-physics software tools provides a practical acoustic prediction tool uniquely tailored towards the complexities and intricacies of predicting launch vehicle lift-off acoustic environments.

Application of this approach includes estimation of rocket exhaust noise intensity in the launch platform, water suppression and ignition over-pressure (IOP) analysis,

Acknowledgements

This research was supported by the NASA Marshall Space Flight Center (MSFC) under the Small Business Technology Transfer Research (STTR) program (Contract No. NNX11C136P). The authors would like to thank the STTR project technical monitor Dr. Louise Strutzenberg (NASA-MSFC) for her guidance and providing Loci/CHEM simulations. The authors also thank Dr. Jeffrey West (NASA-MSFC) and Dr. Gabriel Putnam (All Points Logistics) for their technical advice and support.

References

[1]Tam, C.K.W., "Supersonic Jet Noise," *Ann. Rev. Fluid Mech*., 27, pp. 17-43, 1995.

[2]Eldred, K., "Acoustic Loads Generated by the Propulsion System," NASA SP-8072, June 1971.

[3]Counter, D. D., "Computer Program for Predicting Vehicle Acoustic Environment," NASA Memorandum ED33/49-88, George C. Marshall Space Flight Center, May 5, 1988.

[4]Ffowcs Williams, J. E. and Hawkings, D. L., "Sound Generation by Turbulence and Surfaces in Arbitrary Motion," Proceedings of Royal Society London, Vol. 264, 1969, pp. 321–342.

[5]Tam, C.K.W., and Webb, J.C., "Dispersion-Relation-Preserving Finite Difference Schemes for Computational Acoustics," J. Computational Physics, Vol. 107, Issue 2, pp. 262-281, 1993.

[6]Tam, C.K.W., "Computational Aeroacoustics: An Overview of Computational Challenges and Applications," Int. J. Computational Fluid Dynamics, Vol. 18 (6), pp. 547-567, 2004.

[7]Sandham, N.D., and Suponitsky, V., "Contributions to Jet Noise from Instability Waves and their Interactions: From Theory to Modeling," Procedia Engineering 00, pp. 1-10, 2010.

[8]Chandler-Wilde, S.N., Langdon, S., and Ritter, L., "A High-Wavenumber Boundary-Element Method for an Acoustic Scattering Problem," Phil. Tans: Mathematical, Physical and Engineering Sci., Vol. 362, No. 1816, pp. 647-671, 2004.

[9]Bapat, M.S., Shen, L., and Liu, Y.J., "Adaptive Fast Multipole Boundary Element Method for Three-Dimensional Half-Space Acoustic Wave Problems," Eng. Analysis with Boundary Elements, 33, pp. 1113-1123, 2009.

[10]Duran, M., Nedelec, J.-C., and Ossandon, S., "An Efficient Galerkin BEM to Compute High Acoustic Eigenfrequencies," J. Vib. Acoust., Vol 131, Issue 3, 2009.

[11]Pan F., Uzun, A., and Lyrintzis, A., "Surface Integral Methods in Jet Aeroacoustics: Refraction Corrections," AIAA Journal of Aircraft, Vol. 45, No. 2, March-April 2008, pp. 381-387.

[12]Luke, E., and Cinnella, P., "Numerical Simulations of Mixtures of Fluids Using Upwind Algorithms," Computers and Fluids, Volume 36, December 2007, pp. 1547-1566.

[13]Liu, Y.J., Fast Multipole Boundary Element Method - Theory and Applications in Engineering, Cambridge University Press, Cambridge, 2009.

[14]Uzun, A., and Hussaini M.Y,. "Noise Generation in the Near-Nozzle Region of a Chevron Nozzle Jet Flow," 13th AIAA/CEAS Aeroacoustics Conference, AIAA-2007-3596.

[15]Khalighi, Y., Ham, F., Moin, P., Lele, S.K., Schlinker R.H., Reba, R.A., and Simonich, J., "Noise Prediction of Pressure-Mismatched Jets Using Unstructured Large Eddy Simulation," Proceedings of ASME Turbo Expo 2011, Vancouver, Canada, GT2011-46548.

[16]Frigo, M., and Johnson, S.G., "The Design and Implementation of FFTW3," Proceedings of the IEEE 93 (2), 216–231, 2005.

[17]Krothapalli, A., Choutapalli, I., Alkislar, M.B., and Lourenco, L.M., "Aeroacoustics of Twin Supersonic Impinging Jets", AIAA Paper 2003-3316, 9th AIAA/CEAS Aeroacoustics Conference, May 2003.

[18]Tam, C.K.W., Viswanathan, K., Ahuja, K.K., and Panda, J., "The Sources of Jet Noise: Experimental Evidence," J. Fluid Mech., Vol. 615, pp. 253-292, 2008.

[19]Cox, J. S., Brentner, K. S. and Rumsey, C. L., "Computation of Vortex Shedding and Radiated Sound for a Circular Cylinder: Subcritical to Transcritical Reynolds Numbers, Theoret. Comput. Fluid Dynamics, 12: 233–253, 1998.

[20]Revell, J. D., Prydz, R. A., and Hays, A. P., "Experimental study of airframe noise vs. drag relationship for circular cylinders," Lockheed Report 28074, 1977. Final Report for NASA Contract NAS1-14403.

[21]Henderson, B., Bridges, J., and Wernet, M.: "An Investigation of the Flow Structure of Tone Producing Supersonic Impinging Jets", AIAA Paper 2002-2529.

[22]Henderson, B., Bridges, J. and Wernet, M., "An experimental study of the oscillatory flow structure of tone-producing supersonic impinging jets," J. Fluid Mech., vol. 542, pp. 115–137, 2005.

[23]Luke, E., "A Rule-Based Specification System for Computational Fluid Dynamics," Ph.D. Dissertation, Mississippi State University, December, 1999.

[24]Seiner, J.M., Ponton, M.K., Jansen, B. J., and Lagen, N. T., "The Effects of Temperature on Supersonic Jet Noise Emission," DGLR/AIAA 14th Aeroacoustics Conference, Aachen, Germany, AIAA Paper 92–02–046, May 1992.

[25]Manoha, E., Redonnet, S., Delahay, C,. Sagaut, P, Mary, I., Khelil, S.B., and Guillem, P., "Numerical Prediction of the Unsteady Flow and Radiated Noise from a 3D Lifting Airfoil," RTO AVT Symposium on "Ageing Mechanisms and Control: Part A – Developments in Computational Aero- and Hydro-Acoustics," Manchester, UK., 2001.

[26]Biancherin, A., Lupoglazoff, N., Rahier, G., and Vuillot, "Comprehensive 3D Unsteady Simulations of Supersonic and Subsonic Hot Jet Flow-Fields. Part 2: Acoustic Analysis," 8th AIAA/CEAS Aeroacoustics Conference & Exhibit Agenda, AIAA-2002-2600.

[27]Khalighi, Y., Ham, F., Moin, P., Lele, S.K., Schlinker R.H., Reba, R.A., and Simonich, J., "Noise Prediction of Pressure-Mismatched Jets Using Unstructured Large Eddy Simulation," Proceedings of ASME Turbo Expo 2011, Vancouver, Canada, GT2011-46548.

[28]Lighthill, M. J., "On Sound Generated Aerodynamically: I. General Theory," Proc. of the Royal Society of London, Series A: Mathematical and Physical Sciences, 211(1107), 564–587, 1952.

[29]Uzun, A., Lyrintzis, A.S., Blaisdell, G.A., "Coupling of Integral Acoustics Method with LES for Jet Noise Prediction", Intl. J. Aeroacoustics, Vol. 3, No. 4, pp. 297-346, 2004.